



## Original Article

In-situ oxide scale investigation of Sm-doped ZrB<sub>2</sub>/SiC Billets

A.E. Brenner, R.W. Trice\*

Purdue University, West Lafayette, IN 47907, USA



## ARTICLE INFO

## Keywords:

Hypersonic  
Samarium  
Zirconium diboride  
Ablation

## ABSTRACT

Samarium-doped zirconium diboride/silicon carbide (Sm-ZBS) ceramics possess an emittance of 0.9 at 1600 °C and develop oxide scales that have excellent ablation performance. This study investigates the oxide scale development of 3 mol% doped Sm-ZBS which contains 80 vol% ZrB<sub>2</sub> and 20 vol% SiC when exposed to temperatures in excess of 1800 °C in an oxidizing atmosphere. Samples were prepared via chemical infiltration of samarium nitrate into spray-dried powders of 80 vol.% ZrB<sub>2</sub>/20 vol.% SiC; powders were then pressed into billets and sintered without pressure. Samples cut from these billets were then oxidized for 10, 60, and 300 s, respectively, using an oxyacetylene torch. A Sm-depletion region was observed and believed to form due to glass transport to the surface. X-ray diffraction was used to determine the sequence of oxidation of Sm-ZBS, beginning with the formation of ZrO<sub>2</sub> and Sm<sub>2</sub>O<sub>3</sub>. The final oxide scale was determined to be c<sub>1</sub>-Sm<sub>0.2</sub>Zr<sub>0.8</sub>O<sub>1.9</sub>, with a melting temperature exceeding 2500 °C. SEM and EDS were also used to investigate microstructural formation due to the bursting of convection cells.

## 1. Introduction

Sharp leading-edge designs for hypersonic vehicles improve performance by reducing aerodynamic drag. However, sharp edges lead to convective heating resulting in temperatures exceeding 2000 °C [1]. Ultra-high temperature ceramics (UHTC) are among the materials being considered for leading edges, specifically ZrB<sub>2</sub>-SiC (ZBS) which has a high melting point, thermal conductivity, and thermal shock resistance at temperatures of 1500 °C and above [2–4].

Studies performed by Tan et al. [3,5] have shown that adding samarium (Sm) dopant to the ZBS system increases the emittance compared to ceramics comprised only of ZBS. Specifically, in a study where the total hemispherical emittance was tested on a 5 mol% Sm-doped ZBS plasma sprayed coating, it was found to have an emittance of 0.9 at 1600 °C [3]. In addition, the Sm dopant improved ablation performance by forming a stable oxide scale of c<sub>1</sub>-Sm<sub>0.2</sub>Zr<sub>0.9</sub>O<sub>1.9</sub> (SZO) which has a melting point above 2500 °C, making it capable of withstanding extreme temperature conditions during hypersonic flight. Sm was also found to incorporate lower the viscosity SiO<sub>2</sub> phase form via the oxidation of SiC [6]. Similar studies where rare-earth borides and oxides (e.g. LaB<sub>6</sub>, La<sub>2</sub>O<sub>3</sub>, or Gd<sub>2</sub>O<sub>3</sub>) were added to the ZrB<sub>2</sub>/SiC system were also shown to form stable, dense oxide scales of Re<sub>2</sub>Zr<sub>2</sub>O<sub>7</sub> (Re = La, Gd) [7]. These rare-earth zirconates also have high melting temperatures, and were shown to have excellent oxidation resistance. However, ZBS samples containing La<sub>2</sub>O<sub>3</sub> and Gd<sub>2</sub>O<sub>3</sub> were only tested up to 1600 °C in

a furnace [7]. A study performed by Zhang et al. [8], using oxyacetylene ablation testing showed that adding LaB<sub>6</sub> to ZBS also showed excellent oxidation resistance up to 2400 °C.

The motivation of this work is to understand the microstructural evolution of the oxide layer during rapid heating in air, as the formation sequence of the oxide scale of Sm-doped ZBS is not understood. In this study, the oxide scale of 3 mol% Sm-doped ZBS billets ablated using an oxyacetylene torch were evaluated after 10, 60, and 300 s, where maximum temperatures of 1494 °C, 1656 °C, and 1870 °C, respectively, were reached. A dopant concentration of 3 mol.% Sm was chosen as this concentration was shown to create a stable and relatively pore free SZO layer by Tan et al. [3]. The phase assemblage and microstructure as a function of ablation time were analyzed using XRD, SEM, and EDS.

## 2. Experimental procedure

## 2.1. Materials and powder preparation

Spray-dried powders were prepared from a suspension that consisted of 80 vol.% ZrB<sub>2</sub> (3–5 μm, Grade A, HC Starck, Munich, Germany), 20 vol.% α-SiC (1.4 m, Grade UF-05, HC Starck, Munich, Germany), 0.4 wt.% dispersant (Darvan 821A, R.T. Vanderbilt Company, Inc., Norwalk, USA), 2 wt.% PVA binder (Celvol 203, Celanese Corporation, Dallas, USA) and DI water. Spray drying was performed by Arch Instant Spray Drying Services, Brunswick, GA. The

\* Corresponding author at: 701 West Stadium Avenue, West Lafayette, IN 47907, USA.

E-mail address: [rtrice@purdue.edu](mailto:rtrice@purdue.edu) (R.W. Trice).

<https://doi.org/10.1016/j.jeurceramsoc.2019.08.014>

Received 19 April 2019; Received in revised form 10 August 2019; Accepted 14 August 2019

Available online 16 August 2019

0955-2219/ © 2019 Elsevier Ltd. All rights reserved.

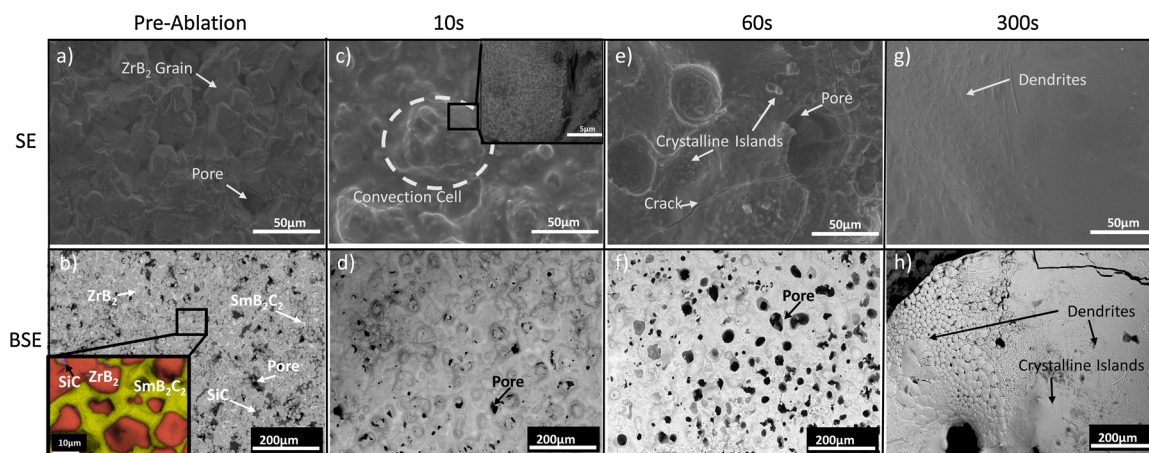


**Fig. 1.** SEM micrographs at different magnifications for pre-ablated billets, 10 s post ablated, 60 s post ablated, and 300 s post ablated. The magnified excerpt image in b) shows  $ZrB_2$  grains (red) surrounded by  $SmB_2C_2$  matrix (yellow) with little patches of SiC (purple). Excerpt BSE image in c) shows the magnified surface of the convection cell containing oxide islands dispersed in a glassy phase (For interpretation of the references to colour in this figure legend, the reader is referred to the web version of this article).

average spray-dried particle size was  $\sim 50 \mu m$ . Samarium dopant was added to the spray dried  $ZrB_2/SiC$  powders via a chemical infiltration method. In this process, 10 mol.% samarium nitrate hexahydrate (99.9% pure  $Sm(NO_3)_3 \cdot 6H_2O$ , Sigma-Aldrich, St. Louis, USA) was dissolved into isopropyl alcohol and the resulting solution was then infiltrated into the porous spray-dried  $ZrB_2/SiC$  powder. Next, the solvent was removed via a rotary evaporator (BM 200, Yamato Scientific America Inc., Santa Clara, USA) at  $100^\circ C$ . This powder was heated at  $400^\circ C$  in air for an hour to remove residual moisture and nitrates. Tan et al. [3] showed that for heating to  $\sim 400^\circ C$  neither the ZBS or Sm-doped powders showed any weight gain. As the normalized weight gain was approximate zero below  $400^\circ C$ , it suggests that the oxidation of the powders has little effect during the heat treatment at  $400^\circ C$ . The first weight gain inflections start near  $600^\circ C$  due to the oxidation of  $ZrB_2$  to form  $m-ZrO_2$  and  $B_2O_3$  glass [3].

Subsequently, the dried mixture was crushed and sieved using a -325 mesh ( $44 \mu m$  aperture) to eliminate large agglomerates. The powder was then pressed into  $38 mm \times 38 mm \times 5 mm$  billets at 679 kPa at room temperature and sandwiched between two SiC plates layered with graphite and sprayed with boron nitride. The purpose of the SiC plates was to avoid bloating of the samples due to outgassing during sintering. Boron nitride was sprayed on the graphite to avoid reaction of the samples with the SiC plate. The pressed billets were then sintered in argon at  $2000^\circ C$  for 15 min (Series System VI, Centorr Vacuum Industries, Nashua, USA). A 1-hr hold at  $1650^\circ C$ , prior to reaching  $2000^\circ C$ , was programmed into the heating cycle to evaporate the boron glass formed from the boron nitride [9]. The billets were sintered to  $87 \pm 2\%$  of the theoretical density of  $6.36 g/cm^3$ . Density measurements were made via the Archimedes' method. During sintering, the billets shrank  $\sim 20\%$  in the length and width dimensions, and  $\sim 40\%$  in the thickness dimension. Billets were then cut to  $25.4 mm \times 25.4 mm$  and polished using an automatic polisher (GPX Series Advanced Autopolisher, LECO Corp., St. Joseph, USA) to an  $R_a$  of  $0.4 \pm 0.1 \mu m$  which was measured via atomic force microscopy (AFM) (Dimension 5000 AFM, Bruker, Santa Barbara, USA). The composition of the billets, as measured by mass spectroscopy, was 29.8 mol% Zr, 56.7% B, 7% C, 0.5% Si, 3% Sm, 2.8% O, and 0.2% impurities (NSL Analytical Services Inc., Cleveland, USA).

## 2.2. Oxyacetylene ablation testing

Ablation resistance was assessed using an oxyacetylene ablative torch rig as performed in previous studies [5]. The test rig was constructed using ASTM 285-082 as a standard [10]. The ablation torch

(Victor Technologies, St. Louis, USA) used a 5 mm orifice and a separation distance of 20 mm between the sample and the torch tip which was kept constant. Front face temperature as a function of time was measured using a one-color pyrometer (OS3750, Omega Engineering Inc., Stamford, CT, USA) which was connected to a data logger while the back-face temperature was measured using a thermocouple. The emittance setting for the pyrometer was set to 0.9. An oxygen rich environment was simulated using an oxygen:acetylene ratio of 12:10 slpm. Test specimens were exposed to the flame for 10, 60, and 300 s. The heat flux was measured to be  $452 W/cm^2$  using a thermogage circular foil heat flux gauge (TG1000-4, Vatell Corp., Christiansburg, VA).

## 2.3. Microstructural and phase analysis

Before performing the microstructural analysis, the samples were coated with a thin layer of Au/Pd. A scanning electron microscope coupled with energy dispersive spectroscopy (SEM-EDS) (Quant 650 FEG, Thermo Fischer Scientific, Hillsboro, USA) was used to characterize coating topography in the as-sprayed conditions as well as after each cycle. X-ray diffraction (XRD) (D8 Focus, Bruker Corporation, Billerica, USA) was used to investigate the phases present.  $Cu K\alpha$  radiation was used over  $2\theta$  values of  $20^\circ - 80^\circ$  on the coatings after ablation using a step size of  $0.02^\circ$  and a scan rate of  $5^\circ/minute$ . Samples were aligned in the XRD to analyze the regions where the ablation flame was most intense. AFM (Dimension 500 AFM, Bruker, Santa Barbara, USA) was used to measure the pre-ablated average surface roughness ( $R_a$ ) of the specimens over a  $300 + \mu m^2$  area in contact mode using a speed of 350 points/second.

## 3. Results

### 3.1. Pre-ablated microstructure and phase assemblage

Fig. 1a show the pre-ablated microstructure of the 87% dense ceramic billet. As expected, there are porous and dense regions visible. Fig. 1b shows the BSE image of the pre-ablated billet which contains several distinct phases correlating to  $ZrB_2$ ,  $SmB_2C_2$ , and SiC as seen in XRD (Fig. 2a). The increased magnification inset image in Fig. 1b shows the  $ZrB_2$  grains are surrounded  $SmB_2C_2$  with some SiC noted. In Fig. 2a the predominant phase is  $ZrB_2$ , with small peaks correlating to the  $SmB_2C_2$  matrix. A small ZrC peak is also visible in the pre-ablated XRD scan. The oxidation of the SiC to SiO and CO during sintering, coupled with the degradation of  $Sm_2O_3$  from the pre-sintered powders in the reducing atmosphere providing the oxygen for the oxidation of SiC, is

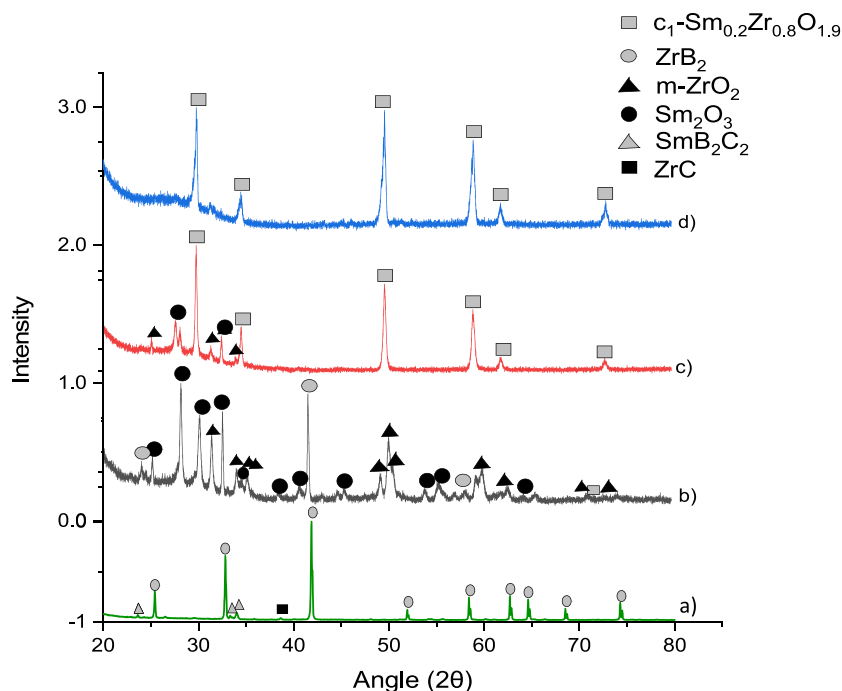


Fig. 2. XRD of a) pre-ablated billets and post-ablated billets after b) 10 s, c) 60 s, and d) 300 s.

believed to result in the formation of the ZrC, SmB<sub>2</sub>C<sub>2</sub>, and loss of SiC in the billets. Similar reactions also occurred with pressureless sintered Y<sub>2</sub>O<sub>3</sub>/SiC [11].

### 3.2. Weight gain and heating profile as a function of ablation time

Fig. 3 shows the front-face sample temperature as a function of ablation time for 10, 60, and 300 s holds. The temperature reached after 10, 60, and 300 s was 1494 °C, 1656 °C, and 1870 °C, respectively. As the emittance of the oxide scale formed is unknown, the pyrometer emittance setting was set to 0.9 which is believed to be higher than the actual emittance ( $\epsilon$ ) of the oxide. Due to the 0.9  $\epsilon$  set point it is believed the actual temperatures reached are higher than measured by the pyrometer. The weight gained after 10 s, 60 s, and 300 s was 0%, 0.8%, and 2.6%, respectively. The inset optical image in Fig. 3b shows a white oxide scale after a 10 s hold, with this surface not much different from

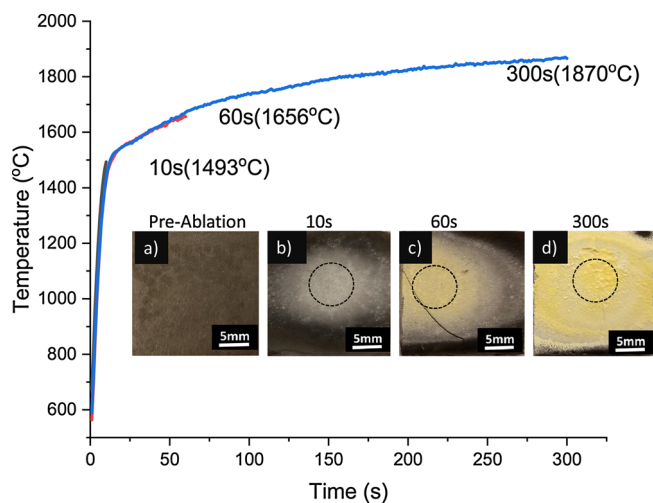


Fig. 3. Time vs. temperature graph of ablated samples 10 s, 60 s, and 300 s. Optical images are a) before ablation, b) 10 s post ablation, c) 60 s post ablation, and d) 300 s post ablation.

the pre-ablated image shown in Fig. 3a. As shown in Figs. 3c (60 s hold) and Fig. 3d (300 s hold) the oxide scale becomes increasingly more yellow as the ablation time increases. It is important to note that the crack in Fig. 3c is a result of excessive force used when billet was removed from the sample holder and is not a result of thermal shock. The dotted circles on the optical images indicate where XRD and SEM/EDS analysis were performed.

### 3.3. Phase make-up after ablation

XRD analysis, presented in Fig. 2b, shows the phases present after 10 s change from ZrB<sub>2</sub> and SmB<sub>2</sub>C<sub>2</sub> to Sm<sub>2</sub>O<sub>3</sub>, and m-ZrO<sub>2</sub> with residual ZrB<sub>2</sub>. A 10 s exposure is sufficient to begin the oxidation process. These oxides of Sm and Zr are expected as their heats of formation are more negative than the borides of the same atom type [12]. Furthermore, the presence of an amorphous hump at low 2θ suggests a glassy phase is present on the surface. As shown in Fig. 2c the phases present on the surface after 60 s of ablation are a c<sub>1</sub>-Sm<sub>0.2</sub>Zr<sub>0.8</sub>O<sub>1.9</sub> (SZO), Sm<sub>2</sub>O<sub>3</sub>, and m-ZrO<sub>2</sub>. XRD results after 300 s, as shown in Fig. 2d, shows a single-crystalline phase, SZO, as well as an amorphous hump.

### 3.4. Microstructure changes with ablation

Figs. 1c–d show the formation of convection cells surrounded by what appears to be a glassy phase after 10 s of ablation. A convection cell is formed through the oxidation of ZrB<sub>2</sub>/SiC to ZrO<sub>2</sub> and borosilicate glass. The Zr- and Sm-doped glass is pushed to the surface from the oxidation of ZrB<sub>2</sub> to ZrO<sub>2</sub>, forming the protrusions on the surface as seen in Fig. 1c–d [13]. These cells burst due to the surge in pressure from the liquid with increased time and heating due to the pressure induced by volume expansion of the oxidation products, which can approach 300% (16) as well as the evaporation of the glass and the oxidation of C (in the SiC) to CO or CO<sub>2</sub>. Once the glass reaches the surface, the borica and silica glass evaporate, and the remaining high concentrations of Zr and Sm can form ZrO<sub>2</sub> and Sm<sub>2</sub>O<sub>3</sub>, respectively. These appear as crystalline phases on the surface. As shown in Fig. 1e–f, the process of oxidation of the ZrB<sub>2</sub>, SiC, and the SmB<sub>2</sub>C<sub>2</sub> continues. The oxidation products were observed deeper below the sample surface

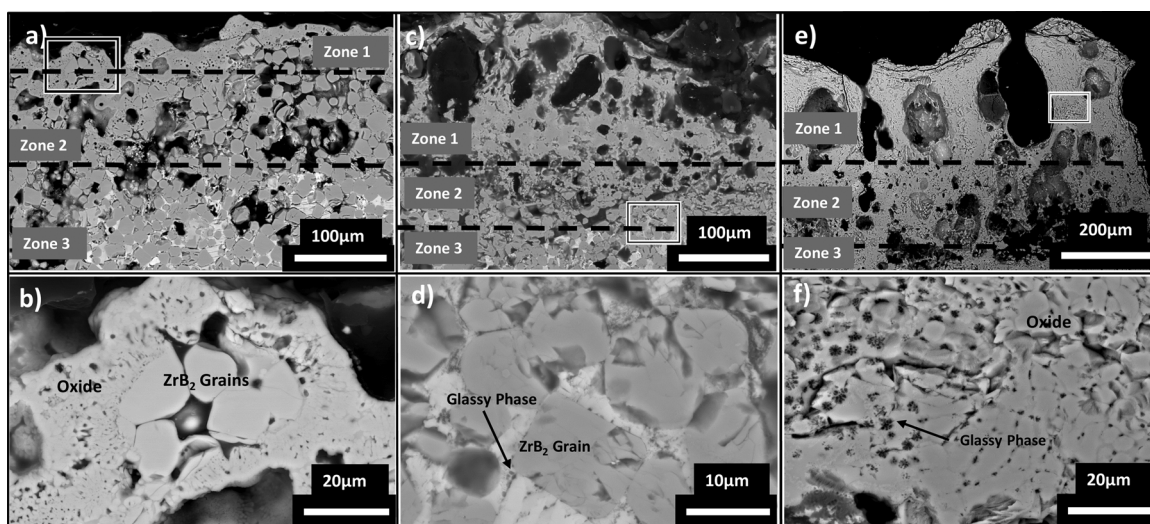


Fig. 4. BSE cross-sectional images of a) 10 s ablated, c) 60 s ablated, and c) 300 s ablated billets. Boxed areas correspond to higher magnified images (images b, d, and f) showing crystalline regions and an intergranular glassy phase.

with time, from ~50 μm below the surface after 10 s to ~150 μm below the surface after 60 s. Also, more glassy phase was observed with time. Eventually the cell bursts due to evaporation of the glass and/or production of CO or CO<sub>2</sub>. This appears to be more prevalent after 60 s. Figs. 1g-h show large pores, indicative of continuing oxidation, along with a large crystalline region present in the topography after 300 s. Large grains and dendrites are visible after 300 s as seen in Fig. 1h indicating a possible eutectic may have occurred between the glass and the crystalline phase [14].

Fig. 4 shows cross-sections of the samples after ablation. These oxide scales form three distinct zones: Zone 1 is the fully developed and reacted oxide scale, Zone 2 is a transition region where oxidation is continuing to occur, and Zone 3 is where the sample has begun to oxidize the SmB<sub>2</sub>C<sub>2</sub> matrix.

EDS analysis of the billets after 10 s, 60 s, and 300 s (see Fig. 5) show differences in the distribution and concentration of Zr, O, and Sm with time and location. After 10 s of ablation, the formation of a thin oxide scale can be seen in Fig. 5 (see Zone 1). The main oxide scale in Zone 1 has a distinct microstructure where both the Zr and Sm appear to be homogeneously mixed compared to Zone 3, which has distinct regions of Zr that maintain the original ZrB<sub>2</sub> square-grain morphology. As shown in Fig. 5, a thin Zone 2 region is also observed after 10 s in that the Zr and Sm regions are still distinct, but the ZrB<sub>2</sub> grain is starting to transform into the oxide. After 60 s of ablation, the primary oxide scale region (Zone 1) has become thicker as evidenced by the complete mixing of the Zr and Sm atoms in this region. XRD results, presented in Fig. 2c, would indicate this region to be primarily SZO. Zone 2 can also be clearly seen as having a similar microstructure to Zone 1, however

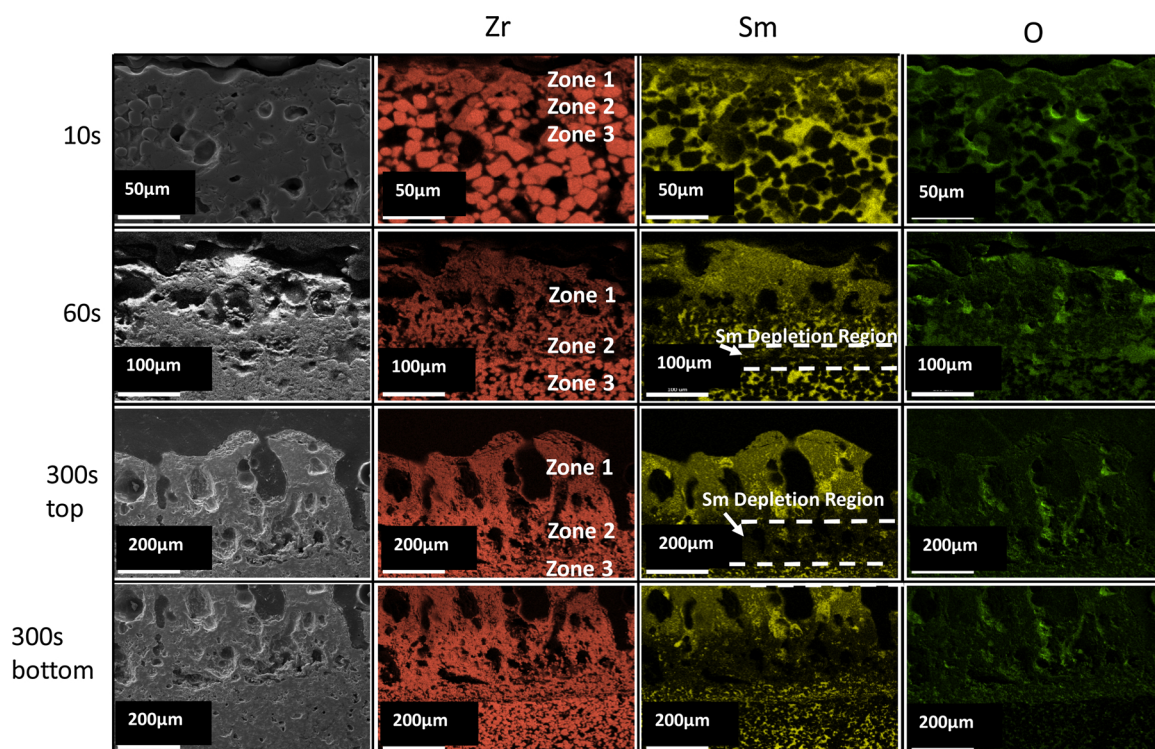


Fig. 5. Cross-sectional EDS analysis of billets after 10 s, 60 s, and 300 s of ablation.

there are still regions of higher concentration of Zr and Sm. It should be noted that EDS shows evidence of small amounts of Sm in the higher Zr concentration regions in Zone 2. Near the bottom of Zone 2 there appears to be a region that is void of Sm atoms deemed a Sm-depletion region, however the high Zr concentration regions in Zone 2 contain  $\sim 2$  at% Sm indicating the Zr is slightly doped. After 60 s of ablation, there is still an unoxidized  $ZrB_2$  region apparent with some oxidation of the  $SmB_2C_2$  matrix (Zone 3). After 300 s of ablation the oxide scale has thickened to where two images (Fig. 5 top and bottom) were needed to reveal microstructural features. After 300 s of ablation, the main oxide scale (Zone 1) can be seen to have become thicker. Zone 2 was also observed to have thickened; a similar Sm atom depletion region was also observed.

## 4. Discussion

### 4.1. First observation: development of the oxide scale morphology as a function of time

#### 4.1.1. Post 10 s of ablation

In Figs. 1c-d, the topographical microstructure after 10 s of ablation consists of partially erupted convection cells. Convection cells like these were observed by Karlsdottir et al. [15] in 15 vol% SiC-85 vol%  $ZrB_2$  that were heated to 1550 °C in air for 1 h. They observed protrusions of islands of  $ZrB_2$  in lagoons of  $SiO_2$  that were a result of viscous fingering created by borosilicate liquid moving up through porous  $ZrO_2$  columns and across a more viscous silica rich fluid. In EDS analysis of our system, B is not evident on the surface. However, this is likely due to the limitations of EDS as well as the high concentrations of the other elements present. Viscous fingering results from the injection of a less viscous liquid into a higher viscous liquid in a porous medium [16]. Although Zr is known to be a substitute for Si or B in glass and increase its viscosity, in small quantities it lowers viscosity [17]. Evidence of the rupture and formation of convective cells can be seen in Fig. 4a and b where angular  $ZrB_2$  grains are transforming into what appears to be a porous oxide as described by Karlsdottir et al. [15]. The formation of the Zr-doped borosilicate glass occurs at a reaction interface, such as a grain boundary [18]. This is the case for our system as well where the reaction interface can be seen in Fig. 4d where the glass is beginning to form at the grain boundaries of  $ZrB_2$ . It was suggested that the driving force for the liquid flow is from the volume increase due to oxidation of  $ZrB_2$  to  $ZrO_2$  [14]. In early oxidative stages, the Zr-rich borosilicate liquid flows through the pores of the primary oxidized  $ZrO_2$  porous layer. Later the volume increase induces pressure and stress leading to the rupture of the oxide scale where the liquid is then squeezed up to the surface and flows to form the convection cells and their features. The rapid evaporation of boria results in rapid formation of precipitated zirconia and rapid formation of convection cells [13]. The inset image in Fig. 1c shows small oxide islands dispersed in the glassy phase on a convection cell. These are believed to be evidence of  $ZrO_2$  and  $Sm_2O_3$  as seen in Fig. 2b. Fig. 6 shows cross-sectional EDS analysis after 10 s of ablation of a  $ZrB_2$  grain nested in a convection cell in Zone 1. Sm-doped Si can be seen between the grains together and the Zr starting to dissolve into the liquid. This confirms the travel path of the liquid. The lack of evidence of boria in Fig. 6 is likely due to the rapid evaporation of this glass. It can also be seen that the oxygen rich region of the columns contains atoms of Zr and Sm. This is indicative of the viscous fingering described in Karlsdottir et al. [15] as well as evidence of the reaction interface for Sm-Zr borosilicate liquid.

#### 4.1.2. Post 60 s of ablation

After 60 s of ablation, it was observed in Fig. 1e-f that the convection cells have erupted and large pores where the convection cells once inhabited populate the surface. When convection cells erupt, this reveals a new path for rapid inward oxygen diffusion, repeating the oxidative process described previously [13]. These pores are also

indicative of the release of gaseous products such as CO or  $CO_2$  and evaporated  $B_2O_3$ . This also reveals a pathway for rapid inward oxygen diffusion and again repeating the formation of evaporated  $B_2O_3$  and CO or  $CO_2$ . This helps explain the increase in oxide scale thickness after 60 s and 300 s of ablation.

It can also be observed in Fig. 1e that the oxide islands are larger. It is hypothesized that the oxide islands grow via two methods. The first is the islands start to coalesce with time. Second is grain growth of SZO from the liquid containing of  $Sm_2O_3$  and  $ZrO_2$  (see section 4.2). As the small grains coalesce and time is increased, rapid grain growth occurs. In Fig. 2c, after 60 s of ablation the main phase present is  $c_1-Sm_{0.2}Zr_{0.8}O_{1.9}$  along with small phases of  $Sm_2O_3$  and  $ZrO_2$ . The large crystalline grains, seen in Fig. 1e, consist of mainly Zr, O, and Sm which correspond to the SZO phase seen in Fig. 2c. A glassy phase consisting of a higher concentration of Sm and Si is also present on the surface which correlates to the amorphous hump seen in Fig. 2c.

#### 4.1.3. Post 300 s of ablation

After 300 s several different microstructural features are present. From the low magnification SEM micrograph in Fig. 1h there are large crystalline regions with large pores which appears to be indicative of coalescence of grains as well as cracks (likely due to thermal shock). Crystalline regions correspond to SZO as it is the only crystalline phase present in Fig. 2d. Cross-sectional results post 300 s of ablation reveal the size of the pores increased with increased ablation time as seen in Fig. 4e. Again, the formation of these pores is due to the buildup of evaporated glass and volatiles as well as from the continual convection cell formation process.

When surface magnification is decreased dendrites, islands, and large grains of SZO are apparent as seen in Fig. 1h. Around each of the mentioned crystalline phases there is a Sm/Si/O glass with a small amount of Zr. Fig. 7 shows Zr, Sm, and Si compositions in different regions of a sample ablated for 300 s. In the large continuously “smooth” crystalline region depicted in Fig. 7d, glass dendrites are present on top of the grain. This suggests there was a low quantity of glass atop the surface of this zone that, when undercooled, formed the dendritic structure. This dendritic glass structure, which is due to undercooling, can also be observed in the zirconia-silica system [19]. In this large region there are also residual pockets of the Sm/Zr/Si/O glass only visible in BSE and EDS images. This suggests the residual glass has a relatively high evaporation temperature. This similar behavior of the glass is also seen in ZBS doped with yttrium where  $Y_2Si_2O_7$  is formed [20]. As seen in Fig. 7c, SZO “islands” are also present in the sample and are surrounded by more of the glassy phase.

Fig. 1h shows these islands appear to gradually form into the large crystalline regions, suggesting their coalescing is the reason for the formation of the large crystalline regions. The large grains are also connected by crystalline dendrites.  $ZrO_2$  dendrites were also observed after an 8-hr furnace hold at 1600 °C [13]. It was suggested that the dendrites precipitated from super-saturation of zirconia in Zr-doped borosilicate liquid, and then coalesced to form the  $ZrO_2$  islands.  $ZrO_2$  crystals deposited via a chemical vapor deposition in atmospheric pressure on a silicon substrate were found to destabilize and form a dendritic structure [21]. It is suggested that the destabilization of the oxide is also the case for our  $c_1-Sm_{0.2}Zr_{0.8}O_{1.9}$  grain edges where a Si-rich amorphous glass is present.

As observed in Fig. 7a-b, there are also regions of round dendrite-like crystals surrounded by doped borosilicate glass. However, this network is different than those in the larger crystalline region. Similar dendrites were also observed in ablated ZBS doped with 5 mol% Sm on an alumina substrate after 2 cycles of ablation [22]. In that study the flower-like dendrites of Sm-stabilized  $ZrO_2$  were formed via the deposition process of Sm/Al-stabilized  $ZrO_2$  precipitating from the lobes of a boria-rich glass surrounded by silica-rich glass [22]. In this system, a flower with petals pattern was not observed for the ablation times investigated. Dendritic structures like these were also seen in liquid

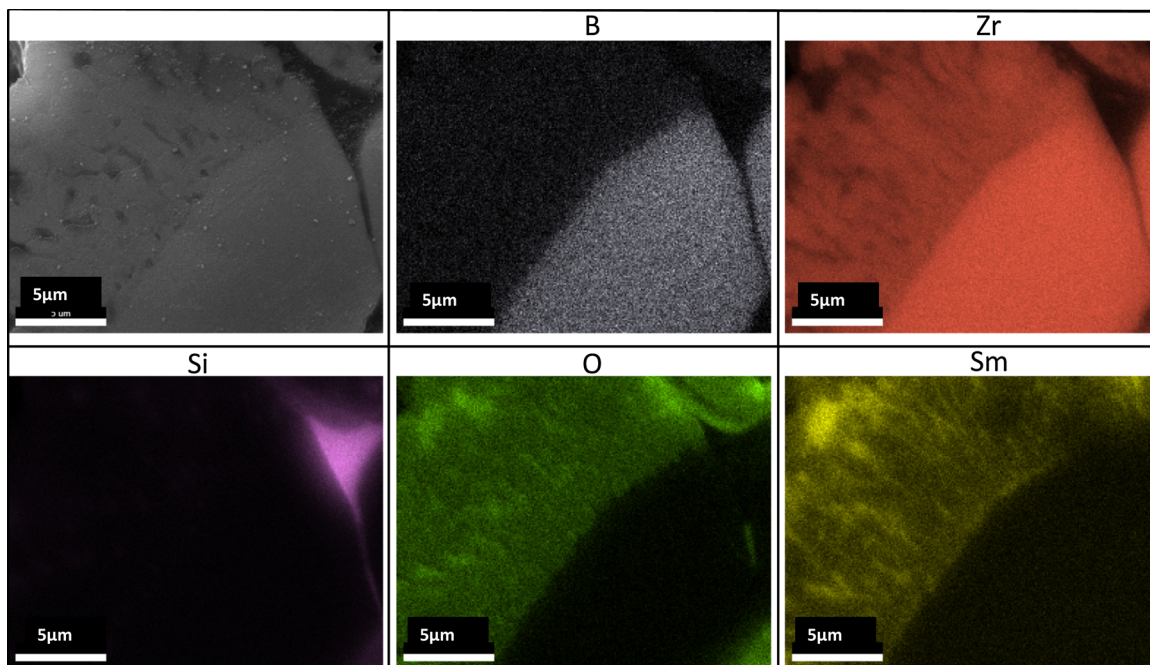


Fig. 6. EDS analysis post 10 s of ablation in Zone 1 of a convection cell that contains an oxidizing ZrB<sub>2</sub> grain as well as the formation of the intergranular Sm-doped silicate glassy phase.

zirconia-silica systems [19]. The dendrites were said to arise as aggregated ZrO<sub>2</sub> surrounded by two liquids of different Zr and Si compositions in turbulent conditions. However, the Zr containing dendrites observed in this study are clearly different than those observed in the previous studies. One possible explanation for the formation of an

eutectic with the oxide and the Si containing glassy phase. The SiO<sub>2</sub>-ZrO<sub>2</sub> phase diagram shows that SiO<sub>2</sub> with 10 mol% ZrO<sub>2</sub> forms a eutectic at 1687 °C [23]. Although we were higher in temperature (1870 °C), we also have Sm in the system. It is suggested that in this crystalline region there was a significant amount of Sm-doped silicate

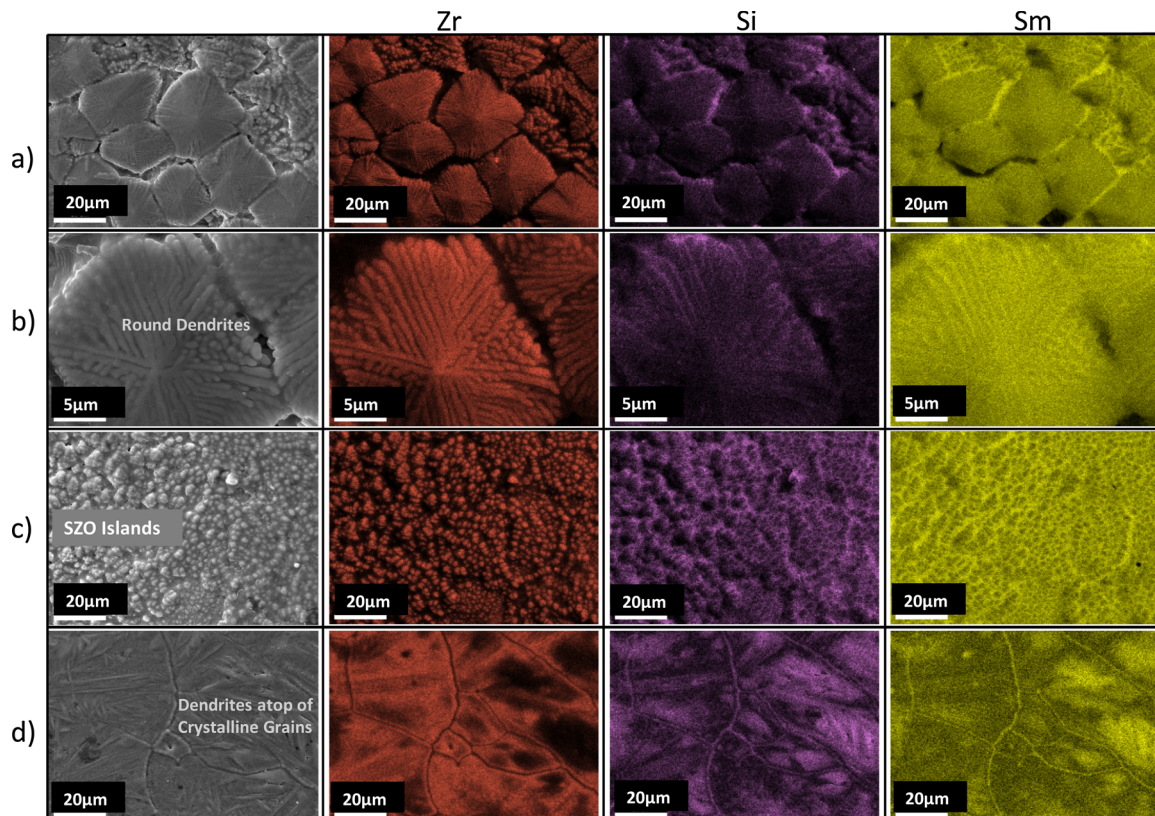


Fig. 7. EDS analysis of post 300 s of ablation of a) round dendrites, b) higher magnification of a), c) oxide island region, and d) large uniform crystalline phase with dendrites on top.

glass on the surface. It is possible the glass reacted with the oxide to destabilize it and form a second liquid.

#### 4.2. Second observation: Sm-doped samples form SZO from Sm<sub>2</sub>O<sub>3</sub> and ZrO<sub>2</sub> and glass transportation

As observed in Fig. 2b and c, Sm<sub>2</sub>O<sub>3</sub> and m-ZrO<sub>2</sub> are present after 10 s and 60 s of ablation and are believed to be the first oxides to form. As shown in Fig. 2, an amorphous hump is also present in the low 2θ region after 10 s, 60 s, and 300 s of ablation indicating the formation of a glassy phase. The oxidation of the starting SmB<sub>2</sub>C<sub>2</sub> matrix and ZrB<sub>2</sub> grains (see Fig. 2a) results in the formation of these two oxides on the surface as well as Sm/Zr-doped B<sub>2</sub>O<sub>3</sub>/SiO<sub>2</sub> (borosilicate) glass and likely gas phases to include CO or CO<sub>2</sub>. After 10 s the SmB<sub>2</sub>C<sub>2</sub> matrix appears to oxidize first in Zone 3 (Fig. 5). After 10 s of ablation the Sm containing matrix is clearly being oxidized as O is only present with the Sm in Zone 3. The Zr rich regions, indicative of the ZrB<sub>2</sub> grain, remain unoxidized. It is believed the Sm diffuses with the oxygen and dopes the Zr-rich region forming partially Sm-doped m-ZrO<sub>2</sub> (as Sm is present in the oxidized Zr region). In Fig. 6 it is clearly seen that the Sm and high O concentrations align in the oxidized portion of the ZrB<sub>2</sub> grain. It can also be seen in the oxidized regions of the grain that the regions rich in Zr are doped with Sm. This is believed to be evidence of the grain transforming into partially Sm-doped m-ZrO<sub>2</sub> and Sm<sub>2</sub>O<sub>3</sub>. Although m-ZrO<sub>2</sub> and Sm<sub>2</sub>O<sub>3</sub> could not be distinguished in EDS analysis on the surface, it is believed they are in the form of nano-oxides in the glassy phase. Small oxide islands of about 500 nm in the inset image in Fig. 1c can be seen dispersed in the glassy phase and are believed to be ZrO<sub>2</sub> and Sm<sub>2</sub>O<sub>3</sub>. This was the case for ablated HfB<sub>2</sub>/SiC ceramics where nano-oxides of HfO<sub>2</sub> were found emulsified in SiO<sub>2</sub> glass [24].

Because of the Sm<sub>2</sub>O<sub>3</sub> in the system studied presently, SZO develops on the surface as observed in XRD results after 60 s (Fig. 2c) as the primary oxide present, and after 300 s as the single crystalline phase present (Fig. 2d). This is due to the reaction of Sm<sub>2</sub>O<sub>3</sub> and ZrO<sub>2</sub>. The Sm<sub>2</sub>O<sub>3</sub>/ZrO<sub>2</sub> phase diagram shows that at 1700 °C ~11 mol% Sm<sub>2</sub>O<sub>3</sub> is needed to react with ZrO<sub>2</sub> to form SZO [25]. Although we only start out with 3 mol% Sm in the system, there is a concentration of 23 mol% Sm on the surface after 300 s of ablation. Tan et al. [5] also found a higher concentration of Sm on the surface of plasma sprayed coatings of Sm-doped ZBS after 60 s of ablation at similar conditions. The increase in Sm is due to the Sm-doped amorphous glassy phase being forced to the surface through the formation, flow, and bursting of convection cells (described more fully in Section 4.1). Cross-sectional analysis in Fig. 5 reveal a depletion region of Sm between Zones 2 and 3 after 60 s of ablation. Zone 2 depicts an active oxidation region compared to Zone 1 where the oxide is finished forming. As the Sm incorporates into the Si rich regions and as the oxidation of ZrB<sub>2</sub> to ZrO<sub>2</sub> occurs (although slightly Sm-doped according to EDS), the Sm is still being pushed up to the surface forming the gap seen in Fig. 5. The formation of this liquid depletion region is also seen in ZrB<sub>2</sub>/SiC and HfB<sub>2</sub>/SiC systems for Si regions [24,18,26]. Evidence of the glass being forced through pores and grain boundaries can be seen after 60 s and 300 s in Fig. 5 from the higher concentration of Sm in Zone 1. The glassy phase located at grain boundaries in Zone 1 are also evident in Fig. 4f. This increase of Sm-doped silica provides enough Sm to form the SZO phase. As the billet is oxidized and B<sub>2</sub>O<sub>3</sub> and SiO<sub>2</sub> (in the form of SiO gas) evaporates the surface, the Sm concentration increases. This evaporation allows for the Sm<sub>2</sub>O<sub>3</sub> and ZrO<sub>2</sub> to react and form SZO.

## 5. Conclusion

The microstructural evolution of ablated samarium-doped zirconium diboride/silicon carbide was investigated to understand the formation of the c<sub>1</sub>-Sm<sub>0.2</sub>Zr<sub>0.8</sub>O<sub>1.9</sub> oxide layer and its constituent components. It was found that SZO phase is formed by first forming oxides of Sm<sub>2</sub>O<sub>3</sub> and ZrO<sub>2</sub> due to the oxidation of ZrB<sub>2</sub> and the samarium

containing matrix. As the Sm incorporates into and transports with the silica glass it forms a depletion region as well as provides enough Sm to form c<sub>1</sub>-Sm<sub>0.2</sub>Zr<sub>0.8</sub>O<sub>1.9</sub> on the surface. The formation of convection cells and the coalescing of the oxides proceeds to have grain growth. Dendritic structures also formed from a possible eutectic with the amorphous phase.

## Acknowledgments

Special thanks to Jorge Ramirez Valesco for assisting in the ablation testing and Andrew Schlup for help with sintering. The authors would also gratefully acknowledge the financial support of Dr. Ali Sayir of the Air Force Office of Scientific Research (AFOSR Grant # FA9550-16-1-0039).

## References

- [1] T.H. Squire, J. Marschall, Material property requirements for analysis and design of UHTC components in hypersonic applications, *J. Eur. Ceram. Soc.* 30 (11) (2010) 2239–2251.
- [2] F. Monteverde, The thermal stability in air of hot-pressed diboride matrix composites for uses at ultra-high temperatures, *Corros. Sci.* 47 (8) (2005) 2020–2033.
- [3] W. Tan, C.A. Petorak, R.W. Trice, Rare-earth modified zirconium diboride high emissivity coatings for hypersonic applications, *J. Eur. Ceram. Soc.* 34 (1) (2014) 1–11.
- [4] M. Tului, G. Marino, T. Valente, Plasma spray deposition of ultra high temperature ceramics, *Surf. Coat. Technol.* 201 (5) (2006) 2103–2108.
- [5] W. Tan, M. Adducci, C. Petorak, A.E. Brenner, R.W. Trice, Effect of rare-earth dopant (Sm) concentration on total hemispherical emissivity and ablation resistance of ZrB<sub>2</sub>/SiC coatings, *J. Eur. Ceram. Soc.* (2016) 1–9.
- [6] W. Tan, M. Adducci, R. Trice, Evaluation of rare-earth modified ZrB<sub>2</sub>-SiC ablation resistance using an oxyacetylene torch, *J. Am. Ceram. Soc.* 97 (8) (2014) 2639–2645.
- [7] D.D. Jayaseelan, E. Zapata-Solvas, P. Brown, W.E. Lee, In situ formation of oxidation resistant refractory coatings on SiC-reinforced ZrB<sub>2</sub> ultra high temperature ceramics, *J. Am. Ceram. Soc.* 95 (4) (2012) 1247–1254.
- [8] X.-H. Zhang, P. H. J.-C. Han, L. Xu, S.-H. Meng, The addition of lanthanum hexaboride to zirconium diboride for improved oxidation resistance, *Scripta Mater.* 57 (2007) 1036–1039.
- [9] S. Zhang, G. Hilmas, W. Farhenholtz, Pressureless Sintering of ZrB<sub>2</sub>-SiC Ceramics, *J. Am. Ceram. Soc.* 91 (1) (2008) 26–32.
- [10] A.S.T.M.E. 285-08, Standard Test Method for Oxyacetylene Ablation Testing of Thermal Insulation Materials, ASTM International, 2008.
- [11] T. Negano, K. Kaneko, Effect of atmosphere on weight loss in sintered silicon carbide during heat treatment, *J. Am. Ceram. Soc.* 83 (11) (2000) 2781–2787.
- [12] E.J. Huber, E.L. Head, C. Holley, The heats of formation of zirconium diboride and dioxide, *J. Phys. Chem.* 68 (10) (1964) 3040–3042.
- [13] S.N. Karlsdottir, J.W. Halloran, Formation of oxide films on ZrB<sub>2</sub>-15vol% SiC composites during oxidation: evolution with time and temperature, *J. Am. Ceram. Soc.* 92 (6) (2009) 1328–1332.
- [14] M.B. Amar, E.G. Poire, Pushing a non-newtonian fluid in a Hele-Shaw cell: from fingers to needles, *Phys. Fluids* (1994) 11 (7) (1999) 1757–1767.
- [15] S.N. Karlsdottir, J.W. Halloran, C.E. Henderson, Convection patterns in liquid oxide films on ZrB<sub>2</sub>-SiC composites oxidized at high temperature, *J. Am. Ceram. Soc.* 90 (9) (2007) 2863–2867.
- [16] H.S. Rabbani, D. Or, Y. Liu, C. Lai, N.B. Lu, S.S. Datta, H.A. Stone, N. Shokri, Suppressing viscous fingering in structured porous media, *PNAS* 19 (2018) 4833–4838.
- [17] R. Karell, J. Kraxner, M. Chromcikova, Properties of selected zirconia containing silicate glasses, *CeramicsSilikaty* 50 (2) (2006) 78–82.
- [18] S.N. Karlsdottir, J.W. Halloran, A.N. Grundy, Zirconia transport by liquid convection during oxidation of zirconium diboride-silicon carbide composite, *J. Am. Ceram. Soc.* 91 (1) (2008) 272–277.
- [19] R. Telle, F. Greffrath, R. Prieler, Direct observation of the liquid miscibility gap in the zirconia-silica system, *J. Eur. Ceram. Soc.* 35 (2015) 3995–4004.
- [20] J. He, Y. Wang, L. Lou, L. An, Oxidation behavior of ZrB<sub>2</sub>-SiC (Al<sub>2</sub>Y) ceramics at 1700 °C, *J. Eur. Ceram. Soc.* 36 (2016) 3769–3774.
- [21] D.B. Epassaka, S. Ohshio, H. Saitoh, Morphological instability of ZrO<sub>2</sub> crystallites formed by CVD technique operated under atmospheric pressure, *J. Mater. Sci.* 38 (2003) 3239–3244.
- [22] A.E. Brenner, A.A. Peña, X.L. Phuah, C. Petorak, B. Thompson, R.W. Trice, Cyclic ablation of high-emissivity Sm-doped ZrB<sub>2</sub>-SiC coatings on alumina substrates, *J. Euro. Ceram. Soc.* 38 (2018) 1136–1142.
- [23] L. Liu, Z. Ma, Z. Yan, S. Zhu, L. Gao, “ZrO<sub>2</sub> formation in ZrB<sub>2</sub>/SiC composite irradiated by laser, *Materials* 8 (2015) 8745–8750.
- [24] D.D. Jayaseelan, E. Zapata-Solvas, C.M. Carney, A. Katz, P. Brown, W.E. Lee, Microstructural evolution of HfB<sub>2</sub> based ceramics during oxidation at 1600–2000 °C, *J. Adv. Appl. Ceram.* 114 (2015) 277–295.
- [25] D. Michel, Y. Rouaux, M. Perez, Y. Jorba, Ceramic eutectics in the systems ZrO<sub>2</sub>-Ln<sub>2</sub>O<sub>3</sub> (Ln=Lanthanide): unidirectional solidification, microstructural and crystallographic characterization, *J. Mater. Sci.* (1980) 61–66.
- [26] F. Monteverde, D. Alfano, R. Savino, Effects of LaB<sub>6</sub> addition on arc-jet convectively heated SiC-containing ZrB<sub>2</sub>-based ultra-high temperature ceramics in high enthalpy supersonic airflows, *Corros. Sci.* 75 (2013) 443–453.